PAPER • OPEN ACCESS

Theory of triangulene two-dimensional crystals

View the article online for updates and enhancements.

2D Materials

Theory of triangulene two-dimensional crystals

R Ortiz[1,2,3,6] , G Catarina[1,4,5,6] and J Fernández-Rossier[4,7,*]

1 Departamento de Física Aplicada, Universidad de Alicante, 03690 San Vicente del Raspeig, Spain
2 Departamento de Química Física, Universidad de Alicante, 03690 San Vicente del Raspeig, Spain
3 Donostia International Physics Center (DIPC), Paseo Manuel de Lardizabal 4, 20018 Donostia-San Sebastián, Spain
4 Theory of Quantum Nanostructures Group, International Iberian Nanotechnology Laboratory (INL), Av. Mestre José Veiga, 4715-330 Braga, Portugal
5 Centro de Física das Universidades do Minho e do Porto, Universidade do Minho, Campus de Gualtar, 4710-057 Braga, Portugal
6 These authors contributed equally.
7 On permanent leave from Departamento de Física Aplicada, Universidad de Alicante, 03690 San Vicente del Raspeig, Spain.
* Author to whom any correspondence should be addressed.

E-mail: joaquin.fernandez-rossier@inl.int

Abstract

Equilateral triangle-shaped graphene nanoislands with a lateral dimension of n benzene rings are known as $[n]$triangulenes. Individual $[n]$triangulenes are open-shell molecules, with single-particle electronic spectra that host $n-1$ half-filled zero modes and a many-body ground state with spin $S = (n-1)/2$. The on-surface synthesis of triangulenes has been demonstrated for $n = 3, 4, 5, 7$ and the observation of a Haldane symmetry-protected topological phase has been reported in chains of $[3]$triangulenes. Here, we provide a unified theory for the electronic properties of a family of two-dimensional honeycomb lattices whose unit cell contains a pair of triangulenes with dimensions n_a, n_b. Combining density functional theory and tight-binding calculations, we find a wealth of half-filled narrow bands, including a graphene-like spectrum (for $n_a = n_b = 2$), spin-1 Dirac electrons (for $n_a = 2, n_b = 3$), $p_{x,y}$-orbital physics (for $n_a = n_b = 3$), as well as a gapped system with flat valence and conduction bands (for $n_a = n_b = 4$). All these results are rationalized with a class of effective Hamiltonians acting on the subspace of the zero-energy states that generalize the graphene honeycomb model to the case of fermions with an internal pseudospin degree of freedom with C_3 symmetry.
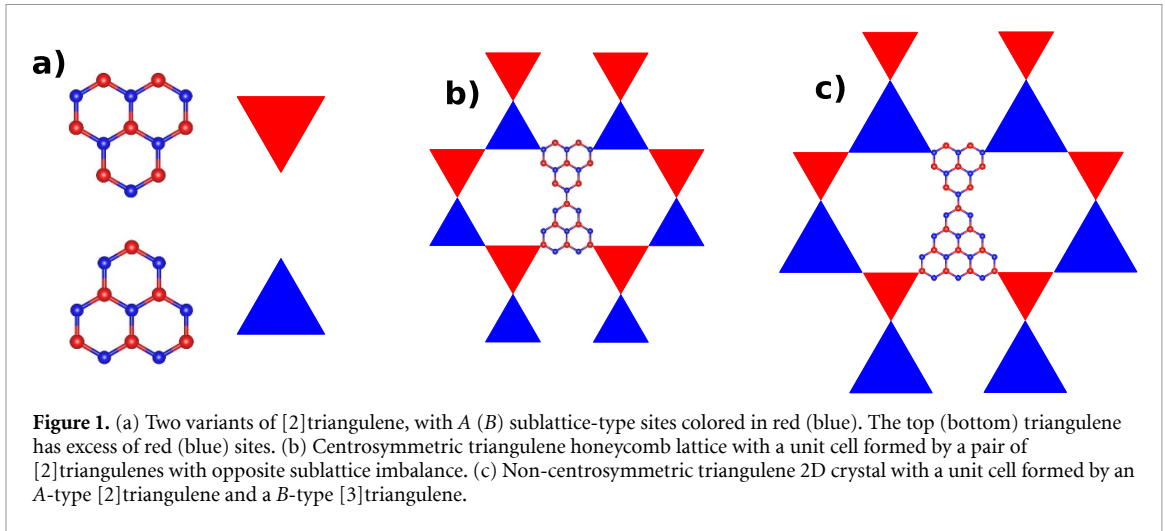
1. Introduction

The quest for new states of matter that do not occur naturally in conventional materials fuels the study of artificial quantum lattices in a variety of platforms, including cold atoms [1, 2], trapped ions [3], quantum dots [4, 5], dopants in silicon [6], functionalized graphene bilayer [7], moiré heterostructures [8] and adatoms [9–11]. These systems may work as quantum simulators of both spin and fermionic Hamiltonians, such as the Hubbard model, and are expected to host strongly correlated electronic phases.

Here, we explore the properties of two-dimensional (2D) artificial crystals with triangulenes as building blocks. Triangulenes are open-shell polycyclic aromatic hydrocarbons. Their low-energy degrees of freedom are provided by electrons that partially occupy zero-energy modes inside a large gap

of strongly covalent molecular states formed by π atomic orbitals. In standard conditions, open-shell molecules are very reactive and therefore not suitable for manipulation. However, thanks to the advances in on-surface chemical synthesis [12–14], it has been possible to go around this problem, so that the controlled fabrication of triangulenes of various sizes [15–18], as well as triangulene dimers [19], chains [20], rings [20, 21] and other structures [22], has been recently demonstrated. On the other hand, the on-surface synthesis of large-area carbon-based crystals has also been established [23–25]. Therefore, the synthesis of 2D triangulene crystals seems within reach using state-of-the-art techniques, motivating the present work.

Individual $[n]$triangulenes have a ground state with spin $S = (n-1)/2$, on account of their strong intramolecular exchange [26, 27]. The small

Figure 1. (a) Two variants of [2]triangulene, with *A* (*B*) sublattice-type sites colored in red (blue). The top (bottom) triangulene has excess of red (blue) sites. (b) Centrosymmetric triangulene honeycomb lattice with a unit cell formed by a pair of [2]triangulenes with opposite sublattice imbalance. (c) Non-centrosymmetric triangulene 2D crystal with a unit cell formed by an *A*-type [2]triangulene and a *B*-type [3]triangulene.

spin–orbit coupling of carbon makes their magnetic anisotropy negligible [20, 28]. The intermolecular exchange coupling in [3]triangulene dimers has been determined to be antiferromagnetic [19–21, 29]. Recently reported [20] experimental results show that chains and rings of [3]triangulenes display the key features of the Haldane phase for antiferromagnetically coupled $S = 1$ spins, namely a gap in the excitation spectrum and the emergence of fractional spin-1/2 edge states. Here, we study $[n_a, n_b]$triangulene 2D crystals, i.e. honeycomb lattices with a unit cell made of two triangulenes with dimensions n_a, n_b (see figure 1 for the cases $n_a = n_b = 2$ and $n_a = 2, n_b = 3$).

The rest of this paper is organized as follows. In section 2, we review the electronic properties of individual [*n*]triangulenes. We argue that, based on a nearest-neighbor tight-binding (TB) approximation, $[n_a, n_b]$triangulene 2D crystals should have $n_a + n_b - 2$ *flat* bands at zero energy. In section 3, we calculate the energy spectrum using density functional theory (DFT) and we find $n_a + n_b - 2$ *narrow* bands, in disagreement with the expectations based on the nearest-neighbor TB model. We show that adding a third neighbor hopping to the TB model accounts for the DFT results and is essential to understand the weakly dispersive bands. In section 4, we build a minimal TB model that includes only the zero-energy modes of the triangulenes and the effect of third neighbor hopping, compare it to both DFT and full TB models, and show that it accounts for the energy bands so obtained. These include a graphene-like spectrum for $n_a = n_b = 2$, spin-1 Dirac electrons for $n_a = 2, n_b = 3$, $p_{x,y}$-orbital honeycomb physics for $n_a = n_b = 3$, and a gapped system with flat valence and conduction bands for $n_a = n_b = 4$. In section 5, we address the effect of interactions and the spin physics in triangulene 2D crystals. In section 6, we wrap up and present our conclusions.

2. Electronic properties of [*n*]triangulenes

2.1. Spectrum and symmetries

In this section, we briefly review the electronic properties of individual [*n*]triangulenes. We first consider their single-particle properties, as described with the TB Hamiltonian, considering one orbital per site and nearest-neighbor hopping, *t*. Because of the bipartite character of the lattice, the energy spectrum must be composed of two types of states: finite-energy states, with electron–hole symmetry, and at least $|N_A - N_B|$ zero modes, where $N_{A/B}$ is the number of sites of the A/B sublattice. In the case of [*n*]triangulenes (see figure 2(a) for $n = 2, 3, 4$), $|N_A - N_B| = n - 1$ and we find $n - 1$ zero modes. We can build triangulenes with excess of either *A* or *B* sites (figure 1(a)). We denote their zero mode wave functions by $|a\rangle$ and $|b\rangle$, respectively.

The zero modes are separated from the finite-energy states by a large energy splitting, as shown in figure 2(a). At half filling, relevant for polycyclic aromatic hydrocarbons at charge neutrality, the zero modes are half-filled. Therefore, the low-energy physics of triangulene crystals are expected to be dominated by the electrons occupying the zero-energy states.

We now focus on the wave functions of the zero modes. As we show in figure 2(b), the zero modes are sublattice-polarized, i.e. they have a non-zero weight exclusively in the *majority* sublattice [27, 30]. Because of the degeneracy of the zero modes for $n \geqslant 3$, their representation is not unique. It is extremely useful to choose $|a\rangle$ and $|b\rangle$ as eigenstates of the $R_{2\pi/3}$ counterclockwise rotation operator:

$$R_{2\pi/3}|a\rangle = e^{i\omega_a}|a\rangle, \quad R_{2\pi/3}|b\rangle = e^{i\omega_b}|b\rangle, \quad (1)$$

where $e^{i3\omega_{a,b}} = 1$. We thus have three possible values for the exponents: $\omega_{a,b} = 0, \pm 2\pi/3$.
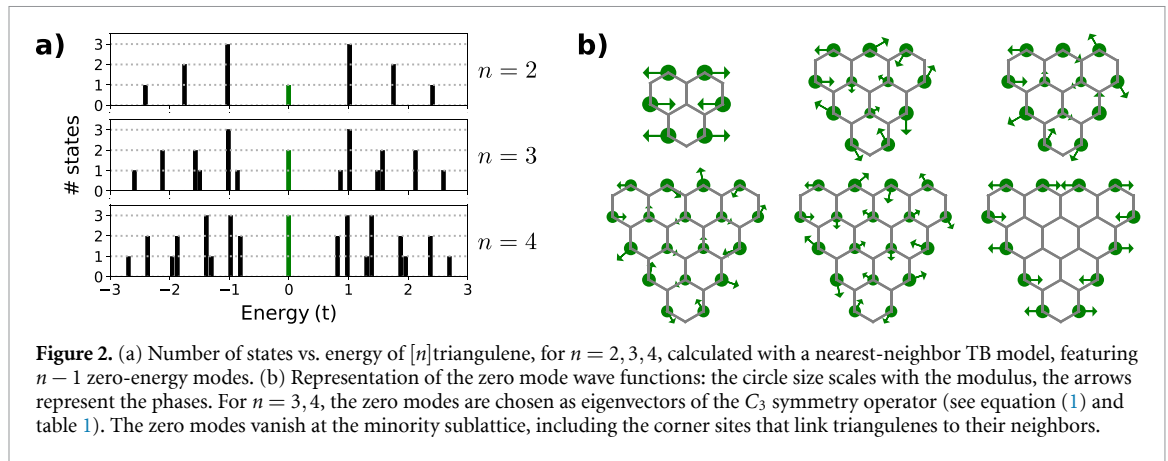
Figure 2. (a) Number of states vs. energy of [n]triangulene, for $n = 2, 3, 4$, calculated with a nearest-neighbor TB model, featuring $n - 1$ zero-energy modes. (b) Representation of the zero mode wave functions: the circle size scales with the modulus, the arrows represent the phases. For $n = 3, 4$, the zero modes are chosen as eigenvectors of the C_3 symmetry operator (see equation (1) and table 1). The zero modes vanish at the minority sublattice, including the corner sites that link triangulenes to their neighbors.

2.2. Interactions and magnetic properties

The $n - 1$ zero modes of [n]triangulenes host $n - 1$ electrons. Therefore, [n]triangulenes have an open-shell structure. Calculations carried out with DFT [27, 31], quantum chemistry [30] and model Hamiltonians [27, 30, 32] consistently predict that the many-body ground state maximizes the spin of the electrons in the zero modes, so that $2S = n - 1$. When modeled with the Hubbard model, the spin of the ground state can be anticipated using Lieb's theorem [33], which states that $2S = |N_A - N_B|$. For [n]triangulenes, $|N_A - N_B| = n - 1$, so that $2S = n - 1$. The underlying mechanism for the ferromagnetic intra-triangulene exchange is a molecular version of the atomic Hund's coupling.

2.3. Intermolecular hybridization of zero modes

Let us now consider the unit cell of a [n_a, n_b]triangulene crystal, i.e. a dimer made of two triangulenes of A and B types. Separately, these triangulenes would have $n_{a/b} - 1$ zero modes each. When coupled together, Sutherland's theorem [34] warrants a minimal number of $|n_a - n_b|$ zero modes per unit cell, and the same number of zero-energy ($E = 0$) flat bands for the corresponding 2D crystal. Specifically, for $n_a = n_b$ the theorem does *not* ensure the existence of $E = 0$ flat bands. However, the binding sites of the unit cell in the triangulene 2D lattice belong to the minority sublattice, whereas the zero modes are hosted in the majority sublattice (figure 2(b)). Therefore, *nearest neighbor hopping does not hybridize zero modes of adjacent triangulenes*. As a consequence, t does not lift the zero mode degeneracy in a [n_a, n_b]triangulene crystal, so that a nearest neighbor TB model predicts $n_a + n_b - 2$ flat bands at zero energy. We anticipate that intermolecular hybridization of zero modes in triangulene 2D crystals will be governed by the small third neighbor hopping, leading to weakly dispersive half-filled energy bands.
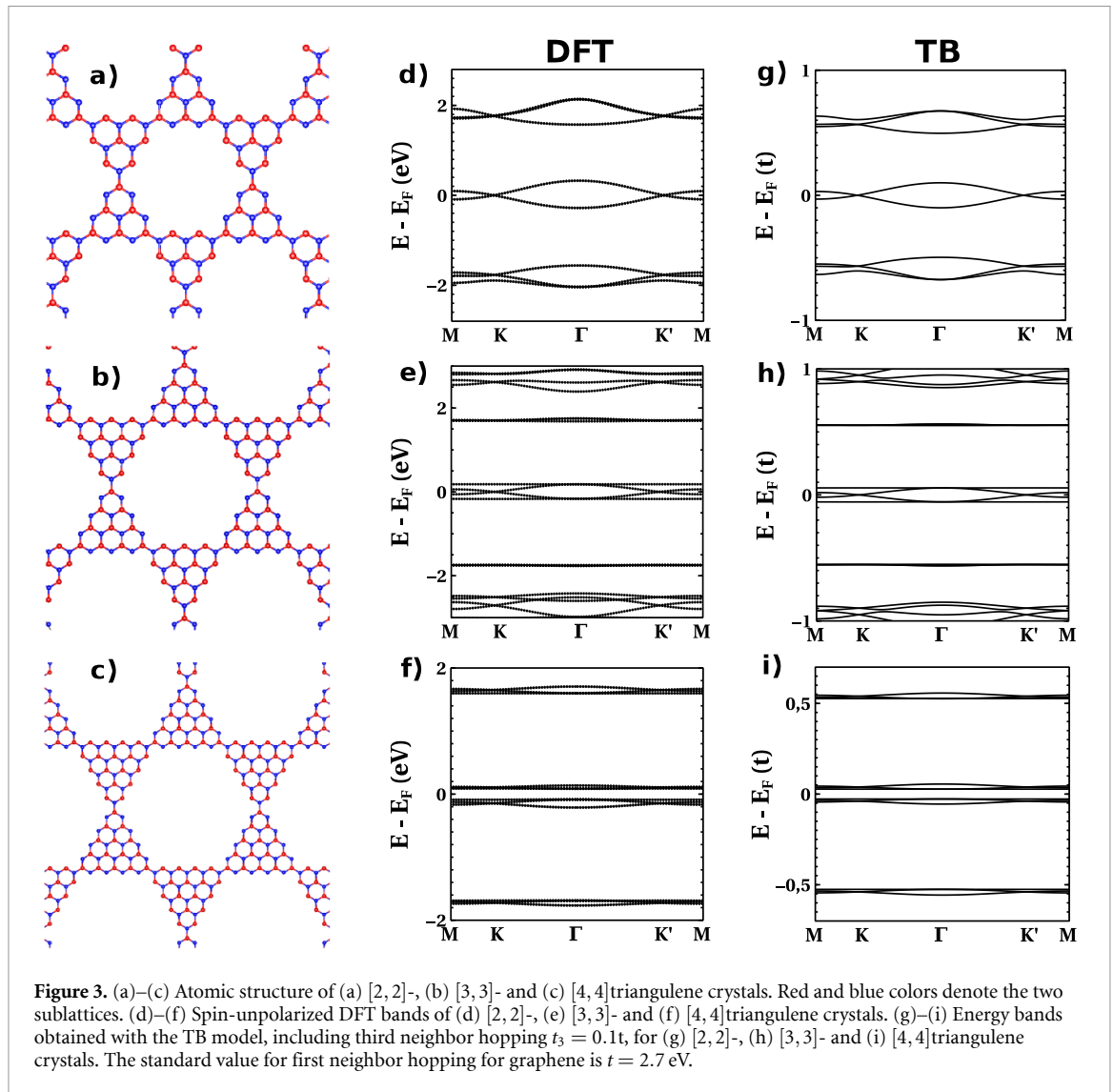
3. Non-magnetic energy bands: DFT vs. TB

We now discuss the energy bands of several [n_a, n_b]triangulene 2D crystals, calculated with two

methods: spin-unpolarized DFT and TB (see results for $n_a = n_b = 2, 3, 4$ in figure 3). Our DFT calculations were carried out with Quantum Espresso [35], using the Perdew–Burke–Ernzerhof functional [36]. The edge carbon atoms were passivated with hydrogen. The kinetic energy cutoff considered was 30 Ry. The charge density and potential energy cutoffs used were 700 Ry. We employed $\vec{k}$-grids of $8 \times 8 \times 1$ for the [3, 3]triangulene crystal and of $10 \times 10 \times 1$ for the [2, 2] and [4, 4] cases. Before the self-consistent calculations, we performed successful relaxation of the cell geometries until the pressure was below 0.5 kbar, obtaining no significant deviations from planarity.

The spin-unpolarized DFT calculations enforce non-magnetic solutions, so that interactions do not break time-reversal nor sublattice symmetry. Below, we show that the resulting low-energy bands are associated with the triangulene zero modes and can be accounted for by the TB calculations, as long as third neighbor hopping is included. We start by addressing the DFT bands obtained for the [2, 2]-, [3, 3]- and [4, 4]triangulene crystals (figures 3(d)–(f)). Our results are in agreement with previous work by the group of Feng Liu [37, 38] for the [2, 2] and [4, 4] cases.

The overall picture of the spin-restricted DFT bands for [n, n]triangulenes, with $n = 2, 3, 4$, is the following. A set of $2(n - 1)$ weakly dispersive bands is located around the Fermi energy, well separated from higher/lower energy bands. Given that the number of zero modes per unit cell is $2(n - 1)$, it can be expected that the wave functions of these bands are mostly made of zero modes. In the case of $n = 2$ (figure 3(d)), the bands are isomorphic to the π bands of graphene, but with a *smaller* bandwidth of 605 meV. The $n = 3$ bands, shown in figure 3(e), feature two Dirac cones and, in addition, two flat bands at the maximum and minimum of the graphene-like Dirac bands. We note that these bands are identical to those obtained in the $p_{x,y}$-orbital honeycomb model [39, 40]. The spectrum of the [4, 4]triangulene crystal (figure 3(f), see also a zoom in figure 5(g)) features a small gap of 0.17 eV, with flat valence/conduction bands and a pair of graphene-like bands whose top (bottom) is degenerate with the valence (conduction) flat band at

Figure 3. (a)–(c) Atomic structure of (a) $[2,2]$-, (b) $[3,3]$- and (c) $[4,4]$triangulene crystals. Red and blue colors denote the two sublattices. (d)–(f) Spin-unpolarized DFT bands of (d) $[2,2]$-, (e) $[3,3]$- and (f) $[4,4]$triangulene crystals. (g)–(i) Energy bands obtained with the TB model, including third neighbor hopping $t_3 = 0.1t$, for (g) $[2,2]$-, (h) $[3,3]$- and (i) $[4,4]$triangulene crystals. The standard value for first neighbor hopping for graphene is $t = 2.7$ eV.

the Γ point. We note that the same set of bands was found in crystalline networks where topological zero-energy states are hosted at the junctions of a network of graphene nanoribbons [41].

The appearance of non-dispersive bands at finite energy is quite peculiar, as non-bonding states in bipartite lattices usually correspond to sublattice-polarized modes with $E = 0$. Here, the sublattice-polarized $E = 0$ states seem to hybridize, forming pairs of bonding–antibonding states that lead to electron–hole symmetric bands, some of which being flat bands with finite energy. The origin of the peculiar dispersion of these low-energy bands, expected to be all flat at $E = 0$ in the nearest-neighbor TB model, is addressed in the next section.
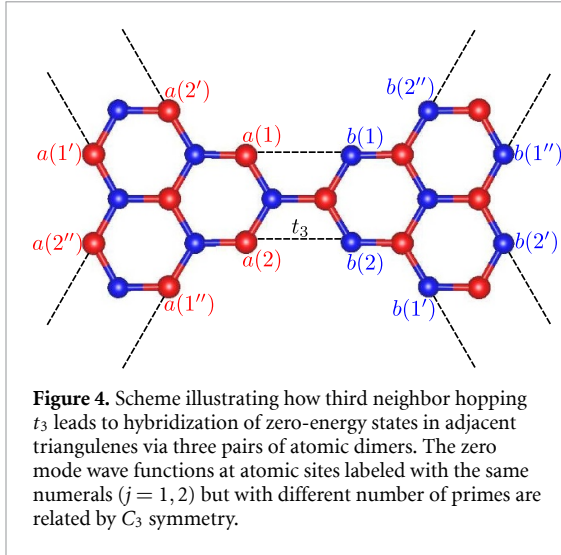
The dispersion of the low-energy bands obtained with DFT suggests that the zero modes of adjacent triangulenes do hybridize, so that the nearest neighbor TB approximation fails. Second neighbor hopping does not couple states hosted at different sublattices, including the zero modes of adjacent triangulenes, and leads to bands that break electron–hole symmetry. Therefore, it is natural to consider a

third neighbor hopping, t_3. Our calculations with $t_3 = 0.1t$ show energy bands in qualitative agreement with those of DFT for the $[2,2]$-, $[3,3]$- and $[4,4]$triangulene crystals (figures 3(g)–(i)). If we take $t_3 = 0$ (not shown), the $n_a + n_b - 2$ low-energy bands become flat, with $E = 0$. Thus, we conclude that third neighbor hopping accounts for the observed dispersion and is the key energy scale that controls inter-triangulene hybridization.

4. Effective low-energy theory

The TB results of the previous section illustrate that $[n_a, n_b]$triangulene 2D crystals provide a platform to generate a wide class of non-trivial energy bands, including graphene-like Dirac dispersion, $p_{x,y}$-orbital honeycomb physics and a gapped system with flat valence and conduction bands. The emergence of these peculiar results calls for a deeper comprehension.

In order to ascertain the ultimate origin of the peculiar properties of the low-energy bands of $[n_a, n_b]$triangulenes, we define an effective

Figure 4. Scheme illustrating how third neighbor hopping t_3 leads to hybridization of zero-energy states in adjacent triangulenes via three pairs of atomic dimers. The zero mode wave functions at atomic sites labeled with the same numerals ($j = 1, 2$) but with different number of primes are related by C_3 symmetry.

Table 1. From left to right: size of the triangulene, labels for the corresponding $n - 1$ zero-energy modes, phase that each zero mode wave function acquires upon the action of the $R_{2\pi/3}$ operator (see equation (1) and figure 2(b)), and values of each zero mode wave function at the binding sites $j = 1, 2$. The label z stands for either a or b.

n	zero mode	ω_z	$z(1)$	$z(2)$
2	z_0	0	$\frac{1}{\sqrt{6}}$	$\frac{-1}{\sqrt{6}}$
3	z_+	$+\frac{2\pi}{3}$	$\frac{1}{\sqrt{11}}$	$\frac{-1}{\sqrt{11}}$
3	z_-	$-\frac{2\pi}{3}$	$\frac{1}{\sqrt{11}}$	$\frac{-1}{\sqrt{11}}$
4	z_0	0	$\frac{1}{\sqrt{12}}$	$\frac{-1}{\sqrt{12}}$
4	z_+	$+\frac{2\pi}{3}$	$\frac{1}{\sqrt{21}}$	$\frac{-1}{\sqrt{21}}$
4	z_-	$-\frac{2\pi}{3}$	$\frac{1}{\sqrt{21}}$	$\frac{-1}{\sqrt{21}}$

Hamiltonian in terms of the $n_a + n_b - 2$ zero modes in the unit cell, calculated with the TB model with $t_3 = 0$.[8] These zero modes are split into two groups consisting of $n_a - 1$ $|a\rangle$ and $n_b - 1$ $|b\rangle$ states localized in the A and B sublattices of adjacent triangulenes, respectively. Third neighbor hopping connects $|a\rangle$ and $|b\rangle$ at three pairs of atomic dimers at the corners of the triangulenes (figure 4). On the other hand, t_3 does not couple zero modes of the same triangulene, as they belong to the same sublattice. The resulting effective model defines a honeycomb lattice with $n_a + n_b - 2$ states per unit cell, whose Bloch Hamiltonian can be written as:

$$\mathcal{H}_{\text{eff}}(\vec{k}) = \begin{pmatrix} 0^{[a]} & \tau(\vec{k}) \\ \tau^\dagger(\vec{k}) & 0^{[b]} \end{pmatrix}, \quad (2)$$

where $\vec{k}$ denotes the 2D crystal momentum, $0^{[a/b]}$ are square matrices of dimension $n_{a/b} - 1$ with all entries equal to zero, and τ is an $(n_a - 1) \times (n_b - 1)$ rectangular matrix with entries given by:

$$\tau_{ab}(\vec{k}) = \sum_{m=0,1,2} e^{i\vec{k}\cdot\vec{R}_m} t_{ab}^{(m)}. \quad (3)$$

In the previous expression, $\vec{R}_0 = (0, 0)$ is the null vector associated to the intracell hopping terms, and $\vec{R}_{1,2}$ are the primitive vectors that define the hexagonal lattice of $[n_a, n_b]$ triangulenes:

$$\vec{R}_{1,2} = (n_a + n_b + 1)\vec{a}_{1,2}, \quad (4)$$

where $\vec{a}_{1,2}$ are the primitive vectors of the graphene hexagonal lattice. The ($\vec{k}$-independent) hopping matrix elements $t_{ab}^{(m)}$ are defined below. As usual, the hopping between A and B states of the honeycomb lattice has one intracell (the $m = 0$ term of the sum in

equation (3)) and two intercell (the $m = 1, 2$ terms of the sum in equation (3)) contributions.

The intracell hopping matrix elements can be expressed as:

$$t_{ab}^{(0)} = t_3 \sum_{j=1,2} a(j)b^*(j), \quad (5)$$

where $a(j) = \langle j|a\rangle$ and $b(j) = \langle j|b\rangle$ denote the components of the zero mode wave functions $|a\rangle$ and $|b\rangle$ at the atomic sites $j = 1, 2$, following the labeling depicted in figure 4. Importantly, we can always impose that $a(1) = b(1) \in \mathbb{R}$, from which it follows that $a(2) = b(2) \in \mathbb{R}$. In the following, we shall assume this gauge fixing. For that reason, we will use the notation z for cases where we want to label either a or b.

Using the point group symmetry of the triangulenes, the intercell hopping matrix elements can be expressed in terms of the intracell ones. Given the values of $z(1)$ and $z(2)$, together with the phases ω_z that each zero mode wave function acquires when applying the $R_{2\pi/3}$ operator (see table 1 for $n = 2, 3, 4$), the remaining values of $z(j')$ and $z(j'')$ can be determined by making use of the C_3 symmetry. Specifically, we use that $z(j) = e^{i\omega_z}z(j') = e^{-i\omega_z}z(j'')$ to obtain:
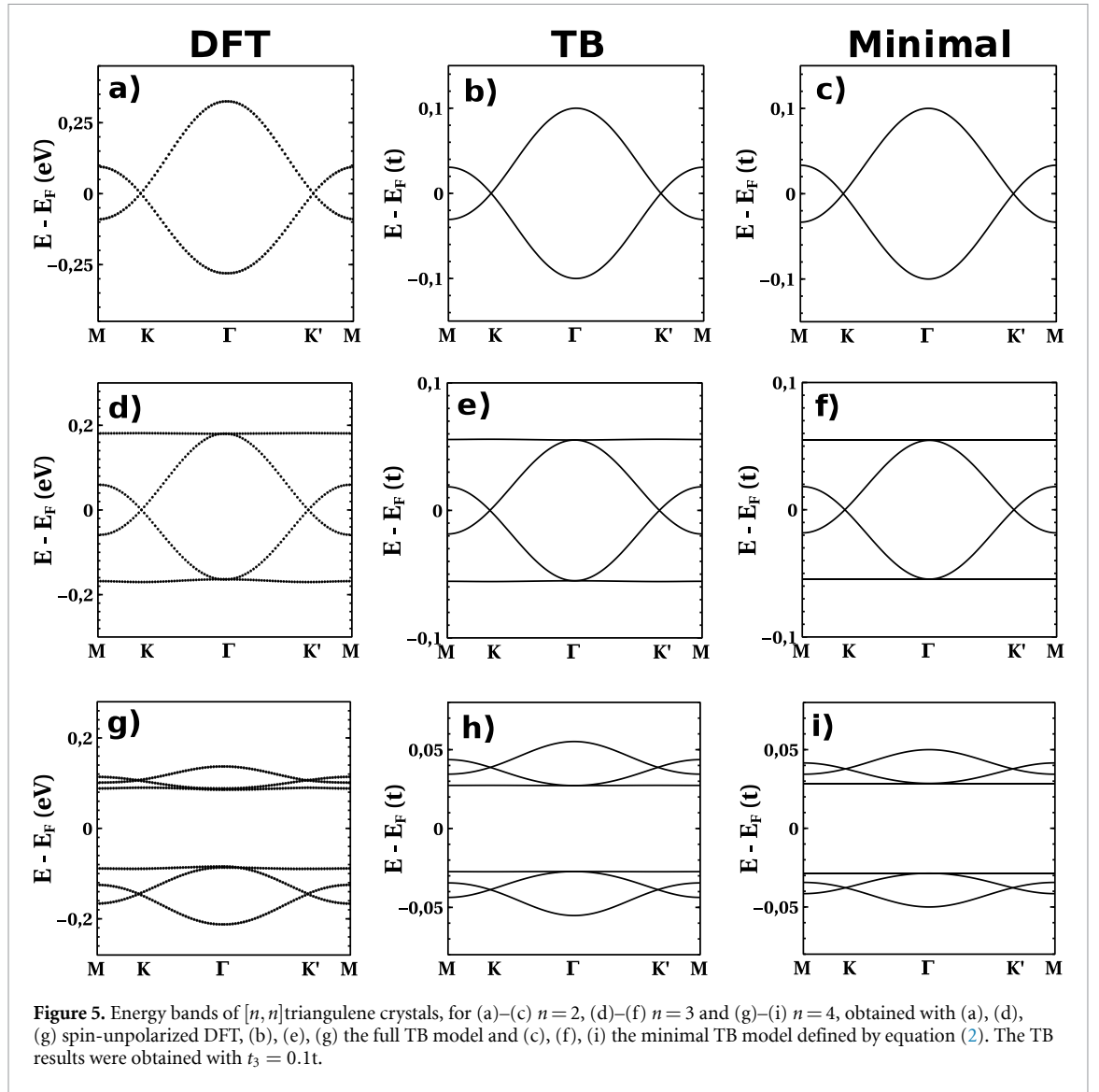
$$t_{ab}^{(1)} = t_3 \sum_{j'=1',2'} a(j')b^*(j') = e^{i(\omega_b - \omega_a)}t_{ab}^{(0)} \quad (6)$$

and

$$t_{ab}^{(2)} = t_3 \sum_{j''=1'',2''} a(j'')b^*(j'') = e^{i(\omega_a - \omega_b)}t_{ab}^{(0)}, \quad (7)$$

which fully clarifies how to build the effective Hamiltonian of equation (2).

The effective Hamiltonian described above is the *minimal* TB model that is expected to capture the $n_a + n_b - 2$ narrow bands of $[n_a, n_b]$ triangulenes. This minimal model describes a honeycomb lattice whose unit cell has $n_a - 1$ and $n_b - 1$ states in the A and B sublattice-type sites, respectively. We can think of the different states of the same sublattice as a pseudospin degree of freedom with C_3 symmetry, thereby generalizing the honeycomb model of graphene to the

---

[8] See [42] for a similar derivation applied to a toy model for one-dimensional crystals of [3]triangulenes.

Figure 5. Energy bands of $[n,n]$triangulene crystals, for (a)–(c) $n = 2$, (d)–(f) $n = 3$ and (g)–(i) $n = 4$, obtained with (a), (d), (g) spin-unpolarized DFT, (b), (e), (g) the full TB model and (c), (f), (i) the minimal TB model defined by equation (2). The TB results were obtained with $t_3 = 0.1$t.

case of fermions with an additional internal structure. The magnitude of the effective hopping is controlled by the weight of the zero modes at the intracell binding sites $j = 1, 2$. The intercell hopping matrix elements depend on the phase differences $\omega_a - \omega_b$. When nonzero, we can interpret the phases ω_z as Peierls phases associated to a pseudospin-dependent magnetic field. Importantly, the model must still be time-reversal invariant.

In figures 5(c), (f) and (i), we show the energy bands obtained with the minimal TB model for $n_a = n_b = 2, 3, 4$, taking $t_3 = 0.1$t. We find an excellent agreement with the full TB model (figures 5(b), (e), and (h)), which in turn agrees with the spin-unpolarized DFT results (figures 5(a), (d), and (g)). Below, we take an in-depth look into the effective Hamiltonian of equation (2), which allows us to have a better understanding of the band dispersion for $n_a = n_b = 2, 3, 4$, as well as for the non-centrosymmetric case $n_a = 2, n_b = 3$ (not addressed yet).

4.1. $[2,2]$triangulene crystal

The minimal Hamiltonian for the $[2,2]$triangulene crystal is a 2×2 matrix that is isomorphic to the TB model for a monoatomic honeycomb lattice with one orbital per site and nearest neighbor hopping. The reason for that is the fact that there is only one zero mode per triangulene, with $\omega_z = 0$. Using that $z(1) = -z(2) = \frac{1}{\sqrt{6}}$ (see table 1), we get $t_{ab}^{(0)} = t_{ab}^{(1)} = t_{ab}^{(2)} = t_3/3$. Thus, we obtain the following effective Bloch Hamiltonian:

$$\mathcal{H}_{\text{eff}}^{[2,2]}(\phi_1, \phi_2) = \frac{t_3}{3} \begin{pmatrix} 0 & f(\phi_1, \phi_2) \\ f^*(\phi_1, \phi_2) & 0 \end{pmatrix}, \quad (8)$$

with

$$f(\phi_1, \phi_2) = 1 + e^{i\phi_1} + e^{i\phi_2} \quad (9)$$

and

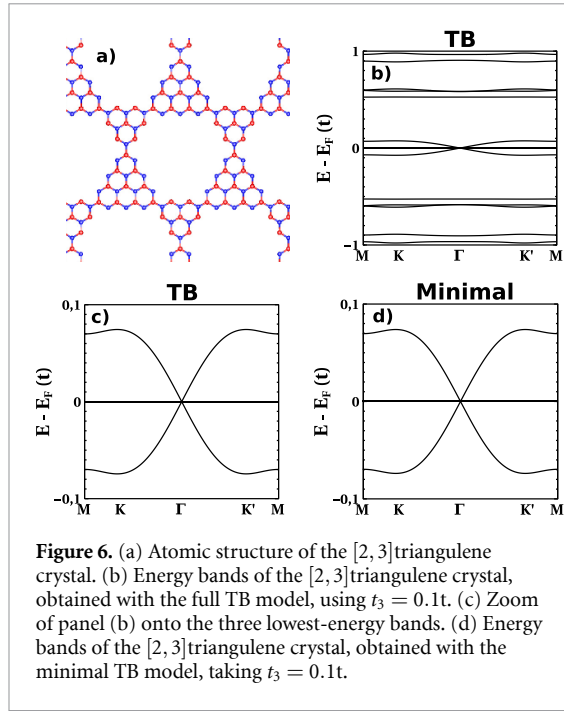$$\phi_{1,2} = \vec{k} \cdot \vec{R}_{1,2}. \quad (10)$$

Figure 6. (a) Atomic structure of the $[2,3]$triangulene crystal. (b) Energy bands of the $[2,3]$triangulene crystal, obtained with the full TB model, using $t_3 = 0.1t$. (c) Zoom of panel (b) onto the three lowest-energy bands. (d) Energy bands of the $[2,3]$triangulene crystal, obtained with the minimal TB model, taking $t_3 = 0.1t$.

The corresponding energy bands are given by:

$$\epsilon_\pm^{[2,2]}(\phi_1, \phi_2)$$

$$= \pm \frac{t_3}{3}|f(\phi_1, \phi_2)|$$

$$= \pm \frac{t_3}{3}\sqrt{3 + 2\cos\phi_1 + 2\cos\phi_2 + 2\cos(\phi_1 - \phi_2)}. \tag{11}$$

The Hamiltonian obtained in equation (8) is identical to the TB model for the p_z orbitals of graphene, but with an effective hopping given by:

$$t_{\text{eff}}^{[2,2]} = \frac{t_3}{3}, \tag{12}$$

which leads to an energy bandwidth of $6t_{\text{eff}}^{[2,2]} = 2t_3$. The bandwidth obtained by our DFT calculations is around 0.6 eV, which implies $t_3 \simeq 0.3$ eV, in line with the values from the literature [43]. A Taylor expansion of equation (8) around the K and K' points yields Dirac cones with Fermi velocity $\hbar v_{\text{F}}^{[2,2]} = \frac{5}{2}t_3 d$, where d denotes the carbon–carbon distance.

In short, we see that third neighbor hopping in $[2,2]$triangulene crystals produces an intermolecular hybridization of the zero modes that leads to the formation of an *artificial graphene* lattice, with a narrower bandwidth governed by t_3, instead of by the nearest neighbor hopping.

4.2. $[2,3]$triangulene crystal

The $[2,3]$triangulene (see figure 6(a)) is the smallest non-centrosymmetric triangulene 2D crystal. It has a sublattice imbalance of $|N_A - N_B| = 1$ that accounts for the presence of one flat band at $E = 0$. Within the minimal model, it has three states per unit cell. Using

the results of table 1, the effective Bloch Hamiltonian can be written as:

$$\mathcal{H}_{\text{eff}}^{[2,3]}(\phi_1, \phi_2)$$

$$= \begin{pmatrix} 0 & \mathcal{F}_{a_0,b_+}^{[2,3]}(\phi_1, \phi_2) & \mathcal{F}_{a_0,b_-}^{[2,3]}(\phi_1, \phi_2) \\ \mathcal{F}_{a_0,b_+}^{[2,3]}{}^*(\phi_1, \phi_2) & 0 & 0 \\ \mathcal{F}_{a_0,b_-}^{[2,3]}{}^*(\phi_1, \phi_2) & 0 & 0 \end{pmatrix}, \tag{13}$$

with

$$\mathcal{F}_{a_0,b_\pm}^{[2,3]}(\phi_1, \phi_2) = \frac{2t_3}{\sqrt{6 \times 11}}f(\phi_1 \pm \theta, \phi_2 \mp \theta) \tag{14}$$

and $\theta = 2\pi/3$. The corresponding eigenvalues read as:

$$\epsilon_0^{[2,3]}(\phi_1, \phi_2) = 0 \tag{15}$$

and

$$\epsilon_\pm^{[2,3]}(\phi_1, \phi_2)$$

$$= \pm\sqrt{\left|\mathcal{F}_{a_0,b_+}^{[2,3]}(\phi_1, \phi_2)\right|^2 + \left|\mathcal{F}_{a_0,b_-}^{[2,3]}(\phi_1, \phi_2)\right|^2}$$

$$= \pm\frac{2t_3}{\sqrt{33}}\sqrt{3 - \cos\phi_1 - \cos\phi_2 - \cos(\phi_1 - \phi_2)}. \tag{16}$$

In figure 6(d), we plot these energy bands, which are verified to yield an excellent agreement with the low-energy bands of the full TB model (figures 6(b) and (c)).

At the Γ point, we have $\phi_1 = \phi_2 = 0$ and therefore $\mathcal{F}_{a_0,b_\pm}^{[2,3]}(0,0) = 0$, which accounts for the triple degeneracy of the bands at that point. A Taylor expansion of equation (13) around Γ leads to the following expression for the dispersive bands:

$$\epsilon_\pm^{[2,3]}(\vec{k}) \simeq \pm 6\sqrt{\frac{3}{11}}t_3 d|\vec{k}|, \tag{17}$$

that accounts for the single Dirac cone. The corresponding Fermi velocity, $\hbar v_{\text{F}}^{[2,3]} = 6\sqrt{\frac{3}{11}}t_3 d$, is larger than that obtained in the $[2,2]$triangulene crystal. It must also be noted that, in the neighborhood of Γ, the minimal Hamiltonian can be mapped into a spin-1 Dirac model [44].

4.3. $[3,3]$triangulene crystal

For $n_a = n_b = 3$, there are two zero modes per triangulene, that we label as $|a_\pm\rangle$ and $|b_\pm\rangle$. The pairs of zero modes $|z_+\rangle$ and $|z_-\rangle$ can be distinguished by the following property: $R_{2\pi/3}|z_\pm\rangle = e^{\pm i2\pi/3}|z_\pm\rangle$. Thus, we can think of the phases $\omega_z = \pm 2\pi/3$ as a pseudospin degree of freedom.

Using the minimal model, the 2×2 hopping matrix of the effective Bloch Hamiltonian reads as:

$$\tau^{[3,3]}(\phi_1, \phi_2) = \begin{pmatrix} \mathcal{F}_{a_+,b_+}^{[3,3]}(\phi_1, \phi_2) & \mathcal{F}_{a_+,b_-}^{[3,3]}(\phi_1, \phi_2) \\ \mathcal{F}_{a_-,b_+}^{[3,3]}(\phi_1, \phi_2) & \mathcal{F}_{a_-,b_-}^{[3,3]}(\phi_1, \phi_2) \end{pmatrix}, \tag{18}$$

where

$$\mathcal{F}^{[3,3]}_{a_+,b_+}(\phi_1,\phi_2) = \mathcal{F}^{[3,3]}_{a_-,b_-}(\phi_1,\phi_2) = \frac{2t_3}{11}f(\phi_1,\phi_2),$$
$$(19)$$

$$\mathcal{F}^{[3,3]}_{a_+,b_-}(\phi_1,\phi_2) = \frac{2t_3}{11}f(\phi_1+\theta,\phi_2-\theta) \qquad (20)$$

and

$$\mathcal{F}^{[3,3]}_{a_-,b_+}(\phi_1,\phi_2) = \frac{2t_3}{11}f(\phi_1-\theta,\phi_2+\theta). \qquad (21)$$

Thus, we see that the *pseudospin conserving* terms lead to the same type of matrix elements than in the conventional honeycomb graphene model, whereas the *pseudospin flip* terms contain additional $\theta = 2\pi/3$ phases.

Diagonalizing the minimal Hamiltonian, we obtain

$$\epsilon^{[3,3]}_{1,\pm}(\phi_1,\phi_2) = \pm 3\, t^{[3,3]}_{\text{eff}}, \qquad (22)$$

that accounts for the flat bands at finite energy, and

$$\epsilon^{[3,3]}_{2,\pm}(\phi_1,\phi_2) = \pm t^{[3,3]}_{\text{eff}}|f(\phi_1,\phi_2)|, \qquad (23)$$

that accounts for the graphene-like bands, with an effective hopping $t^{[3,3]}_{\text{eff}} = 2\,t_3/11$. The dispersive graphene-like bands feature Dirac cones at the K and K' points ($\phi_1 = -\phi_2 = \pm 2\pi/3$), with Fermi velocity $\hbar v^{[3,3]}_F = \frac{21}{11}t_3 d$, which is smaller than those obtained for the $[2,2]$ and $[2,3]$ cases.

The emergence of flat bands at finite energy is remarkable. These bands are associated to states that are localized around any given hexagonal ring in the honeycomb lattice [39–41]. Every unit cell of the $[3,3]$triangulene crystal must contribute with one state to each of the two flat bands. Thus, this makes half a state per triangulene and band. Every triangulene participates in three hexagonal rings in a honeycomb lattice. Therefore, every triangulene contributes with $1/6$ of state per band to a given hexagonal ring. Thus, the six triangulenes that form a ring give rise to one localized state, plus its electron–hole partner. Using numerical diagonalization for finite size clusters, we have verified that, indeed, every hexagonal ring hosts two localized states with energies $\pm 3\, t^{[3,3]}_{\text{eff}}$. These states are bonding, in the sense that both sublattices participate, and are thus different from $E = 0$ flat bands, which are sublattice-polarized.

4.4. [4, 4]triangulene crystal

In contrast to the previous triangulene 2D crystals, the energy bands of the $[4,4]$triangulene feature a gap at half-filling. As in the previous cases, the spin-unpolarized DFT bands close to $E = 0$ are well described both by the full TB Hamiltonian and by the minimal low-energy model, as shown in figures 5(g)–(i). The three topmost valence bands, and their conduction band electron–hole partners,
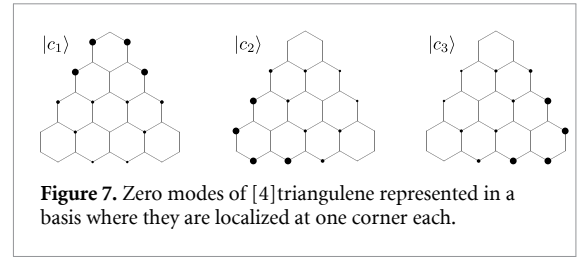

Figure 7. Zero modes of [4]triangulene represented in a basis where they are localized at one corner each.

are identical to the bands of a Kagome lattice: a flat valence/conduction band that is degenerate at the Γ point with the top/bottom of graphene-like bands. The lowest (highest) energy conduction (valence) band is thus dispersionless, which is of particular interest for the field of flat band physics.

Given that for the $[4,4]$triangulene crystal the number of zero modes per triangulene (3) is commensurate with the coordination number of the honeycomb lattice (3), it is natural to associate the bandgap to the formation of an orbital valence bond solid (VBS). This idea is further reinforced by the fact that a gapped band structure is also obtained for the $[7,7]$triangulene crystal, which has 6 zero modes per triangulene. In order to test this idea, and following previous work [41], we build a basis set of zero modes that are localized around one corner. To do so, we take advantage of the isomorphism of the states of a $N = 3$ ring TB model and the three zero modes chosen as eigenstates of the C_3 operator, $|z_0\rangle, |z_\pm\rangle$, that for the sake of this discussion we relabel as $|\omega\rangle$ with $\omega = 0, \pm\frac{2\pi}{3}$, respectively. In the $N = 3$ ring we have:

$$|\omega\rangle = \frac{1}{\sqrt{3}}\sum_{\alpha=1}^{3}e^{i\omega\alpha}|c_\alpha\rangle. \qquad (24)$$

We now invert this equation to obtain the states $|c_\alpha\rangle$ as linear combinations of the C_3 eigenstates. This results in three zero modes peaked around one corner (see figure 7). In the basis of *corner states* $|c_\alpha\rangle$, with $\alpha = 1, 2, 3$, the resulting inter-triangulene Hamiltonians τ_α across the $\alpha = 1, 2, 3$ corners can be *approximately* written as:

$$\tau_1 = \tilde{t}\begin{pmatrix} 1 & \eta & \eta \\ \eta & 0 & 0 \\ \eta & 0 & 0 \end{pmatrix}, \tau_2 = \tilde{t}\begin{pmatrix} 0 & \eta & 0 \\ \eta & 1 & \eta \\ 0 & \eta & 0 \end{pmatrix},$$

$$\tau_3 = \tilde{t}\begin{pmatrix} 0 & 0 & \eta \\ 0 & 0 & \eta \\ \eta & \eta & 1 \end{pmatrix},$$
$$(25)$$

with $\tilde{t} = 0.035t$, $\eta = 0.097$. The terms dropped in these matrices are all order $10^{-2}\tilde{t}$. The dominant $\tilde{t}$ matrix elements correspond to face to face corner states, whereas the $\eta\tilde{t}$ terms correspond to hopping from 'second neighbour corners'. If we had $\eta = 0$, then we would have a dispersionless VBS, where every electron is paired to just one electron. The finite value of η brings about the dispersion.

Analytical expressions for the energy bands can be obtained [41], yielding:

$$\epsilon^{[4,4]}(\phi_1, \phi_2) = \pm \tilde{t}(1 - 2\eta), \ \pm \tilde{t}(1 + \eta \pm \eta \, |f(\phi_1, \phi_2)|). \tag{26}$$

These analytical expressions are in very good agreement with the bands computed by numerical diagonalization of the Hamiltonian without dropping small terms in the τ_α matrices above. We have also verified that the states in the flat bands are also ring states, very much like those of the $[3,3]$ triangulene crystal.

4.5. Overall picture of the single-particle states

The low-energy bands of $[n_a, n_b]$ triangulene crystals are remarkable for several reasons. First, they only disperse because of a third neighbor hopping, that would normally play a residual role, yet it is dominant here. Second, they feature flat bands at finite energy, which are interesting on their own right. Third, they provide a generalization of the honeycomb TB model, with a single orbital per site, to a more general class of honeycomb models where fermions have an internal pseudospin degree of freedom.

At this point, we can draw an analogy between this pseudospin degree of freedom and the orbital angular momentum of atoms, ℓ. For atoms, the orbital degeneracies are given by $2\ell + 1$, with $\ell = 0, 1, 2, \ldots$, and their symmetry properties are governed by the spherical harmonics. For $[n]$ triangulenes, the orbital degeneracies are given by $n - 1$, with $n = 2, 3, 4, \ldots$, and their symmetry properties are determined by the discrete $R_{2\pi/3}$ operator. Very much like the angular momentum wave function of the valence electrons in atoms shapes their electronic properties, the pseudospin of the fermions in $[n_a, n_b]$ triangulene crystals dictates the resulting band structures. In particular, the $[2,2]$ case leads to artificial graphene, $[2,3]$ to the $S = 1$ Dirac Hamiltonian, and $[3,3]$ to the $p_{x,y}$-orbital honeycomb model, all of which featuring Dirac cones at the Fermi energy. The $[4,4]$ triangulene, in contrast, is a band insulator, with flat valence and conduction bands. It must be noted that, even though we have been always considering triangulene 2D crystals at half-filling, other options could be possible if carriers are injected into them, for instance via the application of a gate voltage or through chemical doping [45].

Finally, we note that even though the dispersive low-energy bands are narrow, interactions can turn these systems into Mott insulators at half-filling, as we discuss in the next section.

5. Effect of interactions

5.1. General considerations

We now discuss *qualitatively* the effect of interactions. Unless otherwise stated, we focus on the half filling case. At the single $[n]$ triangulene level, interactions

have a huge impact on the electrons at the zero modes, determining the strong intramolecular ferromagnetic exchange that leads to $2S = n - 1$. In the case of $[n_a, n_b]$ triangulenes, Coulomb repulsion competes with the inter-triangulene hybridization. We quantify this competition in terms of the ratio between two energy scales, that we can define for each zero mode. On the one hand, we have the effective Coulomb interaction,

$$\tilde{U}_a = U \sum_i |a(i)|^4. \tag{27}$$

This effective interaction is thus given by the atomic Hubbard U times the inverse participation ratio (IPR). On the other hand, the average inter-triangulene hopping energy,

$$K_a = \frac{1}{n_b - 1} \sum_b t_{ab}^{(0)}, \tag{28}$$

where $t_{ab}^{(0)}$ is the intracell hopping, given in equation (5), and $n_b - 1$ is the number of zero modes of the n_b triangulene. The average of the ratio $\tilde{U}_a / K_a$ over the a zero modes provides a single figure of merit to quantify the strength of the interactions. The ratios depend both on the values of atomic energy scales U and t_3 and on the properties of the molecular orbitals, $t_{ab}^{(0)}, \tilde{U}_a$.

For instance, in the case of the $[2,2]$ triangulene crystal, with just a single zero mode per triangulene, the IPR of the zero mode is $1/6$, so that the ratio yields $r \equiv \frac{\tilde{U}}{t_{ab}^{(0)}} = \frac{U/6}{t_3/3} = \frac{U}{2t_3}$. For $U = 1.5\,\mathrm{t}$ and $t_3 = 0.1\mathrm{t}$, we have $r \simeq 7.5$, clearly in the insulating side of the metal–insulator transition predicted for $r > 4.5$ for the Hubbard model at half filling in the honeycomb lattice [46]. In the Mott insulating regime, with the charge fluctuations frozen, we expect the $[2,2]$ triangulene crystal to behave like a $S = 1/2$ honeycomb lattice with antiferromagnetic exchange

$$J^{[2]} = 4 \frac{\left(t_{\mathrm{eff}}^{[2,2]} \right)^2}{\tilde{U}} = 6 \times \frac{4}{9} \frac{t_3^2}{U} \simeq 48\,\mathrm{meV}, \tag{29}$$

for $t = 2.7\,\mathrm{eV}$, $U = 1.5\,\mathrm{t}$ and $t_3 = 0.1\mathrm{t}$. As we shall discuss in a forthcoming work [47], in addition to the kinetic exchange, there are other contributions to the antiferromagnetic exchange in this system.

For $[n,n]$ triangulenes with $n = 3, 4, 5$ we find the average of ratios $\tilde{U}_a / K_a$ to be 3.9, 2.9 and 3.1, respectively, if we take typical values [19, 20] of $U = 1.5\,\mathrm{t}$ and $t_3 = 0.1\mathrm{t}$. Thus, interactions cannot be neglected and will very likely drive these systems into a Mott insulating phase.

5.2. Spin-polarized DFT calculations for the $[3,3]$ triangulene crystal

We now discuss the results of our spin-polarized DFT calculations on the $[3,3]$ triangulene crystal. They provide a realistic assessment of the emergence of local moments and their exchange interactions
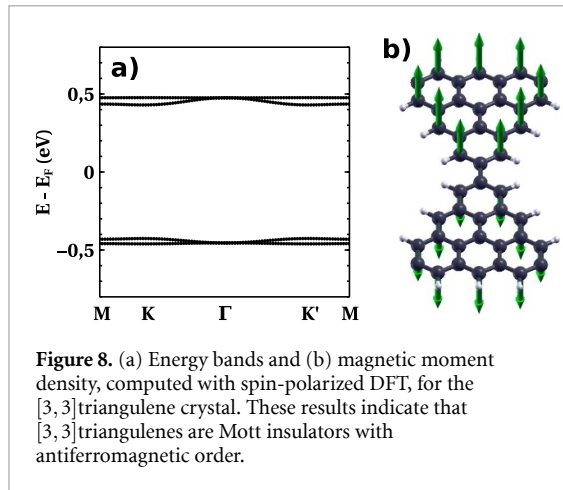
Figure 8. (a) Energy bands and (b) magnetic moment density, computed with spin-polarized DFT, for the [3, 3]triangulene crystal. These results indicate that [3, 3]triangulenes are Mott insulators with antiferromagnetic order.

but can only describe broken symmetry magnetic states, and therefore cannot account for quantum disordered spin phases that are known to occur for one-dimensional (1D) chains of triangulene crystals [20]. The results are shown in figure 8 for the lowest energy magnetic configuration, where the triangulenes have local moments with opposite magnetizations. The four lowest energy bands clearly show that a very large gap has opened where the Dirac bands once stood. Additionally, from the magnetic moments distribution across the molecules, shown in figure 8(b), it is apparent that local moments are hosted by the zero modes. We note that spin-polarized DFT results for the [2, 2]triangulene crystal obtained by Zhou and Liu [37], also feature an antiferromagnetic insulator. Therefore, the available spin-polarized DFT results support the picture that [n, n]triangulenes are Mott insulators with antiferromagnetically coupled local moments.

From our calculations we can infer the value of the intermolecular exchange $J^{[3]}$. For that matter, we compare the energy difference between the ferromagnetic and the antiferromagnetic solutions obtained with DFT, with the result of a classical Heisenberg model. The energy difference per unit cell is given by $6J^{[3]}S^2 = E_{FM} - E_{AFM} = 159.2$ meV. Using $S = 1$ we infer $J^{[3]} = 26.5$ meV. This analysis, that overlooks additional contributions such as biquadratic exchange, is to be compared with the result of $J = 14$ meV, recently inferred for the $S = 1$ triangulene dimer, in the same approximation [19].

5.3. Spin phases in honeycomb crystals
We now briefly discuss the type of interacting ground states that can be expected to arise for the triangulene crystals at half filling. In the case of [2, 2]-crystals, the relevant reference are the quantum Monte Carlo calculations for the Hubbard model in the half filling case. These show a transition to a Neel ordered Mott insulating phase for $U > 4.2$ t. The existence of a spin liquid phase has been studied extensively using Heisenberg spin models [48]. In the case of [2, 3] at half filling, Lieb theorem [33] ensures a ground state

with $S = 1/2$ per unit cell. According to Lieb theorem the non-centrosymmetryc crystals $[n_a, n_b]$ will have a spin $S = |n_a - n_b|/2$ per unit cell, and will be either ferromagnetic or ferrimagnetic.

The $S = 1$ Heisenberg model in the honeycomb lattice has also been studied using density matrix renormalization group calculations in finite size clusters [49]. These calculations predict a Neel phase with long-range order, unless second-neighbor antiferromagnetic interactions, that promote frustration, are significant. For bipartite lattices, second-neighbor exchange coupling would be ferromagnetic. Therefore, a Neel phase is likely to occur for the [3, 3]triangulene crystal at half filling.

In the case of the [4, 4]triangulene crystal, the relevant spin model is the $S = 3/2$ Heisenberg Hamiltonian in the honeycomb lattice with antiferromagnetic interactions. Interestingly, this Hamiltonian is not far from the Affleck–Kennedy–Lieb–Tasaki (AKLT) model for $S = 3/2$, that contains Heisenberg (bilinear) terms as well as biquadratic and bicubic spin couplings [50]. Importantly, the AKLT model can be solved exactly and features a spin VBS. The ground state of the AKLT model is a universal resource for measurement based quantum computing (MBQC) [51]. Importantly, the AKLT model has a gap in the excitation spectrum [52–54], so that cooling down a system described with the AKLT model at low enough temperatures would be enough to prepare a universal resource for MBQC.

The AKLT point is a singular point in a class of models with bilinear and biquadratic couplings, and even bicubic [50] terms in the honeycomb case. In one dimension, the VBS phase is robust in a region of parameters containing both AKLT and the pure Heisenberg limit. For the 2D honeycomb AKLT model, finite-size diagonalization of the spin model [55] found a VBS to Neel transition when AKLT is linearly transformed into a Heisenberg model, but the precise location of the transition is hard to establish due to finite-size effects. In any event, the interesting question of whether the [4, 4]triangulene crystal provides a realization of the VBS in two dimensions remains open. We note that the VBS phase predicted for the $S = 1$ AKLT in one dimension has been observed for [3]triangulene chains [20].

Deviations from half-filling, introducing carriers in the Mott insulating phases, will very likely bring very interesting electronic phases, as it happens in the case of cuprates and in the case of twisted bilayer graphene [56]. This matter deserves further study.

6. Summary and conclusions

We have shown that graphene triangulenes are ideal building blocks for bottom–up design of carbon-based 2D honeycomb crystals with both narrow and flat bands at the Fermi energy. Our study permits to set the rules for the rational design of the

bands, including the number of narrow bands and the presence of flat bands either at the Fermi energy or nearby. The design principles for honeycomb crystals with a unit cell made of two triangulenes, of dimensions n_a, n_b (see figure 1), are:

(a) Isolated $[n]$triangulenes host $n-1$ zero modes that are localized in one sublattice (either a or b, depending on the orientation).

(b) The zero modes vanish identically at the inter-triangulene binding sites. As a result, inter-molecular hybridization is governed by third neighbor hopping t_3.

(c) Centrosymmetric $[n,n]$triangulene crystals have $2(n-1)$ narrow bands. For $n \geqslant 3$ they always feature pairs of electron–hole conjugate low-energy flat bands, corresponding to states localized in supramolecular hexagonal rings. These flat bands are very different from $E=0$ bands, as they are not sublattice polarized and they feature intermolecular hybridization.

(d) Non centrosymmetric $[n_a, n_b]$triangulene crystals, with $n_a \neq n_b$, feature $|n_a - n_b|$ flat bands at $E=0$, because of the bipartite character of the lattice [30, 34].

The results above are validated comparing spin-unpolarized DFT calculations with TB Hamiltonians at two levels: a full-lattice model that includes first and third neighbor hopping and a minimal TB model where only the zero modes of the triangulenes are included. Using the latter approach we are able to derive analytical expressions for the energy bands of the $[2,2]$-, $[2,3]$-, $[3,3]$- and $[4,4]$triangulene crystals.

We have also addressed the effect of electron–electron interactions on these crystals. Both analytical estimates of the relevant energy scales and spin-polarized DFT calculations permit to anticipate that interactions will dominate the electronic properties of these crystals. At half-filling, these crystals are expected to be Mott insulators, with their low energy physics governed by the spin degrees of freedom. Application of Lieb theorem [33], valid for the Hubbard model in bipartite lattices at half filling, permits to anticipate that compensated ($[n,n]$) triangulene crystals have a ground state with $S=0$, and therefore antiferromagnetic intermolecular exchange. We have estimated the magnitude of this super-exchange for the $[2,2]$ and $[3,3]$ crystals, and found very large values, in the range of tens of meV. For non-centrosymmetric $[n_a, n_b]$ crystals with $n_a \neq n_b$, Lieb theorem predicts that the ground state will have $S = |n_a - n_b|/2$ per unit cell. Thus, these crystals will be ferromagnets or ferrimagnets.

Doping these Mott insulators away from half-filling seems an almost certain recipe to discover non-trivial correlated electronic phases. We hope our work, together with recent work showing the great interest of triangulene 1D structures [20], will motivate experimental work to figure out synthetic routes that permit to create triangulene 2D crystals and the exploration of their electronic properties in the lab.

Data availability statement

All data that support the findings of this study are included within the article (and any supplementary files).

ORCID iDs

R Ortiz ⬚ https://orcid.org/0000-0003-3535-0812
G Catarina ⬚ https://orcid.org/0000-0002-7341-0495

References

[1] Hart R A, Duarte P M, Yang T-L, Liu X, Paiva T, Ehsan Khatami E, Scalettar R T, Trivedi N, Huse D A and Hulet R G 2015 Observation of antiferromagnetic correlations in the Hubbard model with ultracold atoms *Nature* **519** 211–4

[2] Mazurenko A Chiu C S, Ji G, Parsons M F, Kanász-Nagy M, Schmidt R, Grusdt F, Demler E, Greif D and Greiner M 2017 A cold-atom Fermi–Hubbard antiferromagnet *Nature* **545** 462–6

[3] Blatt R and Roos C F 2012 Quantum simulations with trapped ions *Nat. Phys.* **8** 277–84

[4] Hensgens T, Fujita T, Janssen L, Xiao Li, Van Diepen C J, Reichl C, Wegscheider W, Das Sarma S and Vandersypen L M K 2017 Quantum simulation of a Fermi–Hubbard model using a semiconductor quantum dot array *Nature* **548** 70–73

[5] Mortemousque P-A, Chanrion E, Jadot B, Flentje H, Ludwig A, Wieck A D, Urdampilleta M, Bäuerle C and Meunier T 2021 Coherent control of individual electron spins in a two-dimensional quantum dot array *Nat. Nanotechnol.* **16** 296–301

[6] Salfi J, Mol J A, Rahman R, Klimeck G, Simmons M Y, Hollenberg L C L and Rogge S 2016 Quantum simulation of the Hubbard model with dopant atoms in silicon *Nat. Commun.* **7** 11342

[7] García-Martínez N A and Fernández-Rossier J 2019 Designer fermion models in functionalized graphene bilayers *Phys. Rev. Res.* **1** 033173

[8] Kennes D M, Claassen M, Xian L, Georges A, Millis A J, Hone J, Dean C R, Basov D N, Pasupathy A N and Rubio A 2021 Moiré heterostructures as a condensed-matter quantum simulator *Nat. Phys.* **17** 155–63

[9] Yang K *et al* 2017 Engineering the eigenstates of coupled spin-1/2 atoms on a surface *Phys. Rev. Lett.* **119** 227206

[10] Khajetoorians A A, Wegner D, Otte A F and Swart I 2019 Creating designer quantum states of matter atom-by-atom *Nat. Rev. Phys.* **1** 703–15

[11] Yang K, Phark S-H, Bae Y, Esat T, Willke P, Ardavan A, Heinrich A J and Lutz C P 2021 Probing resonating valence bond states in artificial quantum magnets *Nat. Commun.* **12** 993

[12] Cai J *et al* 2010 Atomically precise bottom-up fabrication of graphene nanoribbons *Nature* **466** 470

[13] Ruffieux P *et al* 2016 On-surface synthesis of graphene nanoribbons with zigzag edge topology *Nature* **531** 489–92

[14] Jie S, Telychko M, Song S and Jiong L 2020 Triangulenes: from precursor design to on-surface synthesis and characterization *Angew. Chem.* **132** 7730–40

[15] Pavliček N, Mistry A, Majzik Z, Moll N, Meyer G, Fox D J and Gross L 2017 Synthesis and characterization of triangulene *Nat. Nanotechnol.* **12** 308–11

[16] Mishra S *et al* 2019 Synthesis and characterization of π-extended triangulene *J. Am. Chem. Soc.* **141** 10621–5

[17] Su J *et al* 2019 Atomically precise bottom-up synthesis of π-extended [5]triangulene *Sci. Adv.* **5** eaav7717

[18] Mishra S, Kun X, Eimre K, Komber H, Ma J, Pignedoli C A, Fasel R, Feng X and Ruffieux P 2021 Synthesis and characterization of [7]triangulene *Nanoscale* **13** 1624–8

[19] Mishra S *et al* 2020 Collective all-carbon magnetism in triangulene dimers *Angew. Chem. Int., Ed.* **59** 12041

[20] Mishra S *et al* 2021 Observation of fractional edge excitations in nanographene spin chains *Nature* **598** 287–92

[21] Hieulle J *et al* 2021 On-surface synthesis and collective spin excitations of a triangulene-based nanostar *Angew. Chem., Int. Ed.* **60** 25224–9

[22] Cheng S, Xue Z, Can Li, Liu Y, Xiang L, Youqi K, Yan K, Wang S and Ping Y 2022 On-surface synthesis of triangulene trimers via dehydration reaction *Nat. Commun.* **13** 1705

[23] Steiner C, Gebhardt J, Ammon M, Yang Z, Heidenreich A, Hammer N, Görling A, Kivala M and Maier S 2017 Hierarchical on-surface synthesis and electronic structure of carbonyl-functionalized one- and two-dimensional covalent nanoarchitectures *Nat. Commun.* **8** 1–11

[24] Moreno C *et al* 2018 Bottom-up synthesis of multifunctional nanoporous graphene *Science* **360** 199–203

[25] Telychko M *et al* 2021 Ultrahigh-yield on-surface synthesis and assembly of circumcoronene into a chiral electronic Kagome-honeycomb lattice *Sci. Adv.* **7** eabf0269

[26] Ovchinnikov A A 1978 Multiplicity of the ground state of large alternant organic molecules with conjugated bonds *Theor. Chim. Acta* **47** 297–304

[27] Fernández-Rossier J and Palacios J J 2007 Magnetism in graphene nanoislands *Phys. Rev. Lett.* **99** 177204

[28] Lado J L and Fernández-Rossier J 2014 Magnetic edge anisotropy in graphenelike honeycomb crystals *Phys. Rev. Lett.* **113** 027203

[29] Jacob D, Ortiz R and Fernández-Rossier J 2021 Renormalization of spin excitations and Kondo effect in open-shell nanographenes *Phys. Rev. B* **104** 075404

[30] Ortiz R, Boto R Alvarez, García-Martínez N, Sancho-García J C, Melle-Franco M and Fernández-Rossier J 2019 Exchange rules for diradical π-conjugated hydrocarbons *Nano Lett.* **19** 5991–7

[31] Wang W L, Yazyev O V, Meng S and Kaxiras E 2009 Topological frustration in graphene nanoflakes: magnetic order and spin logic devices *Phys. Rev. Lett.* **102** 157201

[32] Güçlü A D, Potasz P, Voznyy O, Korkusinski M and Hawrylak P 2009 Magnetism and correlations in fractionally filled degenerate shells of graphene quantum dots *Phys. Rev. Lett.* **103** 246805

[33] Lieb E H 1989 Two theorems on the Hubbard model *Phys. Rev. Lett.* **62** 1201–4

[34] Sutherland B 1986 Localization of electronic wave functions due to local topology *Phys. Rev.* B **34** 5208–11

[35] Giannozzi P *et al* 2009 QUANTUM ESPRESSO: a modular and open-source software project for quantum simulations of materials *J. Phys.: Condens. Matter* **21** 395502

[36] Perdew J P, Burke K and Ernzerhof M 1996 Generalized gradient approximation made simple *Phys. Rev. Lett.* **77** 3865

[37] Zhou Y and Liu F 2020 Realization of an antiferromagnetic superatomic graphene: Dirac Mott insulator and circular dichroism Hall effect *Nano Lett.* **21** 230–5

[38] Sethi G, Zhou Y, Zhu L, Yang Li and Liu F 2021 Flat-band-enabled triplet excitonic insulator in a diatomic kagome lattice *Phys. Rev. Lett.* **126** 196403

[39] Congjun W, Bergman D, Balents L and Sarma S D 2007 Flat bands and Wigner crystallization in the honeycomb optical lattice *Phys. Rev. Lett.* **99** 070401

[40] Congjun W and Sarma S D 2008 $p_{x,y}$-orbital counterpart of graphene: cold atoms in the honeycomb optical lattice *Phys. Rev.* B **77** 235107

[41] Tamaki G, Kawakami T and Koshino M 2020 Topological junction states and their crystalline network in systems with chiral symmetry: application to graphene nanoribbons *Phys. Rev.* B **101** 205311

[42] Catarina G and Fernández-Rossier J 2022 Hubbard model for spin-1 Haldane chains *Phys. Rev. B* **105** L081116

[43] Tran V-T, Saint-Martin Jérôme, Dollfus P and Volz S 2017 Third nearest neighbor parameterized tight binding model for graphene nano-ribbons *AIP Adv.* **7** 075212

[44] Mizoguchi T, Kuno Y and Hatsugai Y 2021 Flat band, spin-1 Dirac cone and Hofstadter diagram in the fermionic square kagome model *Phys. Rev. B* **104** 035161

[45] Wang T *et al* 2022 Aza-triangulene: on-surface synthesis and electronic and magnetic properties *J. Am. Chem. Soc.* **144** 4522–9

[46] Sorella S and Tosatti E 1992 Semi-metal-insulator transition of the Hubbard model in the honeycomb lattice *Europhys. Lett.* **19** 699

[47] Jacob D and Fernández-Rossier J 2022 Theory of intermolecular exchange in coupled spin-1/2 nanographenes *Phys. Rev. B* **106** 205405

[48] Gong S-S, Sheng D N, Motrunich O I and Fisher M P A 2013 Phase diagram of the spin-1/2 J_1–J_2 Heisenberg model on a honeycomb lattice *Phys. Rev. B* **88** 165138

[49] Gong S-S, Zhu W and Sheng D N 2015 Quantum phase diagram of the spin-1 J_1–J_2 Heisenberg model on the honeycomb lattice *Phys. Rev. B* **92** 195110

[50] Affleck I, Kennedy T, Lieb E H and Tasaki H 1987 Rigorous results on valence-bond ground states in antiferromagnets *Phys. Rev. Lett.* **59** 799–802

[51] Wei T-C, Affleck I and Raussendorf R 2011 Affleck-Kennedy-Lieb-Tasaki state on a honeycomb lattice is a universal quantum computational resource *Phys. Rev. Lett.* **106** 070501

[52] Garcia-Saez A, Murg V and Wei T-C 2013 Spectral gaps of Affleck-Kennedy-Lieb-Tasaki Hamiltonians using tensor network methods *Phys. Rev. B* **88** 245118

[53] Pomata N and Wei T-C 2020 Demonstrating the Affleck-Kennedy-Lieb-Tasaki spectral gap on 2D degree-3 lattices *Phys. Rev. Lett.* **124** 177203

[54] Lemm M, Sandvik A W and Wang L 2020 Existence of a spectral gap in the Affleck-Kennedy-Lieb-Tasaki model on the hexagonal lattice *Phys. Rev. Lett.* **124** 177204

[55] Ganesh R, Sheng D N, Kim Y-J and Paramekanti A 2011 Quantum paramagnetic ground states on the honeycomb lattice and field-induced Néel order *Phys. Rev. B* **83** 144414

[56] Cao Y, Fatemi V, Fang S, Watanabe K, Taniguchi T, Kaxiras E and Jarillo-Herrero P 2018 Unconventional superconductivity in magic-angle graphene superlattices *Nature* **556** 43–50